

Nature of the warm absorber outflow in NGC 4051

Misaki Mizumoto^{1,2★} and Ken Ebisawa^{1,2}

¹*Institute of Space and Astronautical Science (ISAS), Japan Aerospace Exploration Agency (JAXA), 3-1-1 Yoshinodai, Chuo-ku, Sagami-hara, Kanagawa 252-5210, Japan*

²*Department of Astronomy, Graduate School of Science, The University of Tokyo, 7-3-1 Hongo, Bunkyo-ku, Tokyo 113-0033, Japan*

Accepted 2016 December 22. Received 2016 December 22; in original form 2016 August 4

ABSTRACT

The narrow-line Seyfert 1 galaxy NGC 4051 is known to exhibit significant X-ray spectral/flux variations and have a number of emission/absorption features. X-ray observations have revealed that these absorption features are blueshifted, which indicates that NGC 4051 has warm absorber outflow. In order to constrain physical parameters of the warm absorber outflow, we analyse the archival data with the longest exposure taken by *XMM–Newton* in 2009. We calculate the root-mean-square (rms) spectra with the grating spectral resolution for the first time. The rms spectra have a sharp peak and several dips, which can be explained by variable absorption features and non-variable emission lines; a lower ionized warm absorber (WA1: $\log \xi = 1.5$, $v = -650 \text{ km s}^{-1}$) shows large variability, whereas higher ionized warm absorbers (WA2: $\log \xi = 2.5$, $v = -4100 \text{ km s}^{-1}$, WA3: $\log \xi = 3.4$, $v = -6100 \text{ km s}^{-1}$) show little variability. WA1 shows the maximum variability at a time-scale of $\sim 10^4$ s, suggesting that the absorber locates at $\sim 10^3$ times of the Schwarzschild radius. The depth of the absorption features due to WA1 and the observed soft X-ray flux are anticorrelated in several observational sequences, which can be explained by variation of partial covering fraction of the double-layer blobs that are composed of the Compton-thick core and the ionized layer (=WA1). WA2 and WA3 show little variability and presumably extend uniformly in the line of sight. The present result shows that NGC 4051 has two types of the warm absorber outflows; the static, high-ionized and extended line-driven disc winds and the variable, low-ionized and clumpy double-layer blobs.

Key words: galaxies: active – galaxies: Seyfert – X-rays: individual: NGC 4051.

1 INTRODUCTION

NGC 4051 is an archetypical narrow-line Seyfert 1 (NLS1) at $z = 0.0023$ with a mass of $(1.7 \pm 0.5) \times 10^6 M_{\odot}$ (Denney et al. 2009). High-resolution X-ray spectroscopic observations have detected a lot of blueshifted absorption lines in the X-ray energy spectra (see e.g. Collinge et al. 2001; Krongold et al. 2007; Pounds & Vaughan 2011a,b), which indicates presence of the warm absorber outflow with discrete velocity components.

In general, geometry of the warm absorber outflow is difficult to constrain. We can derive the column density ($N_{\text{H}} = n\Delta r$) and the ionization degree ($\xi = L/(nr^2)$) from model fitting, where n is electron number density, Δr is thickness of the absorber, r is location of the absorber and L is the X-ray luminosity. Because these two equations have three unknown values, we cannot solve the problem without some assumptions. For example, King, Miller & Raymond (2012) derived n of the emission-line region from the ratio of triplet emission lines, and constrained n of the warm absorber assuming

that the emission and absorption features originate in the same region. Krongold et al. (2007) estimated n from photoionization equilibrium time-scales. Steenbrugge et al. (2009) derived these values from recombination time-scales. In the end, they elicit very different geometry of outflows.

In order to constrain geometry of the warm absorber outflow, we focus on spectral variability. If we can investigate spectral variability with a high energy resolution, we are able to determine which components are variable and which are not. From characteristic time-scales of the spectral variation, we may constrain location of the multiple absorbers and disentangle their parameters. In order to obtain sufficient photon counts to investigate detailed spectral variability, it is vital that the object is bright enough and has strong absorption features, and that the exposure time is sufficiently long; NGC 4051 is the best target for our analysis because it satisfies all the requirements above.

In this paper, we discuss spectral variability of NGC 4051 with high energy resolution. First, we explain the observations and data reduction in Section 2. In Section 3, we show the data analysis, where the observed energy spectrum requires three different warm absorbers. We see that one warm absorber has a rapid variability,

* E-mail: mizumoto@astro.isas.jaxa.jp

Table 1. Observation IDs, start dates and good exposure times after removing high background periods.

Name	Observation ID	Date	Good exposure
Obs1	0606320101	2009-05-03	31.4 ks
Obs2	0606320201	2009-05-05	29.1 ks
Obs3	0606320301	2009-05-09	15.8 ks
Obs4	0606320401	2009-05-11	15.1 ks
Obs5	0606321301	2009-05-15	21.0 ks
Obs6	0606321401	2009-05-17	26.5 ks
Obs7	0606321501	2009-05-19	22.5 ks
Obs8	0606321601	2009-05-21	29.0 ks
Obs9	0606321701	2009-05-27	26.8 ks
Obs10	0606321801	2009-05-29	14.6 ks
Obs11	0606321901	2009-06-02	43.7 ks
Obs12	0606322001	2009-06-04	20.4 ks
Obs13	0606322101	2009-06-08	24.6 ks
Obs14	0606322201	2009-06-10	23.5 ks
Obs15	0606322301	2009-06-16	29.4 ks

whereas the other absorbers show little variations, from which we constrain location of the absorbers. We discuss origin of the X-ray spectral variability and geometry of the warm absorber outflows of NGC 4051 in Section 4. Finally we show our conclusion in Section 5.

2 OBSERVATION

The *XMM-Newton* satellite (Jansen et al. 2001) observed NGC 4051 15 times during 2009 May–June. Observation IDs, start dates and exposure times are listed in Table 1. The total good exposure time is 334 ks. We used the European Photon Imaging Camera (EPIC)-pn data (Strüder et al. 2001) in the 0.4–12.0 keV band and the reflection grating spectrometer (RGS; Den Herder et al. 2001) in the 0.4–2.0 keV band. EPIC-pn was operated in small window mode. We used the *XMM-Newton* Software Analysis System (*sas*, v.13.5.0) and the latest calibration files as of 2016 January. Their spectra and light curves were extracted with `PATTERN<=4` from the circular regions with 30 arcsec radius centred on the source, whereas background products were extracted from circular regions with 60 arcsec radius within the same CCD chip. High background periods were excluded from both EPIC and RGS data, when the EPIC/pn count rate of the 10–12 keV band with `PATTERN==0` is higher than 0.4 cts s⁻¹. We used `epatplot` to confirm that the pile-up effect is negligible on all the EPIC-pn data set. The RGS data were processed with `rgsproc`. All the spectral fitting were made with `xspec` v.12.8.2 (Arnaud 1996). In the following, the `xspec` model names used in the spectral analysis are explicitly given, the errors are quoted at the statistical 90 per cent level and the cosmological parameters are as follows: $H_0 = 70$ km s⁻¹ Mpc⁻¹, $\Omega_m = 0.27$ and $\Omega_\lambda = 0.73$.

3 DATA ANALYSIS

3.1 Spectral fitting

We stacked all the data and created the time-averaged spectra. The spectral continuum of the EPIC energy band is explained by a power-law component and a soft excess. We fitted the soft excess with the multicolour disc (`diskbb`; Mitsuda et al. 1984), and fitted the power-law component with `cutoffpl`. The EPIC spectrum has a fluorescent Fe-K line at 6.4 keV, therefore we added a reflected component from neutral material (`pexmon`; Nandra

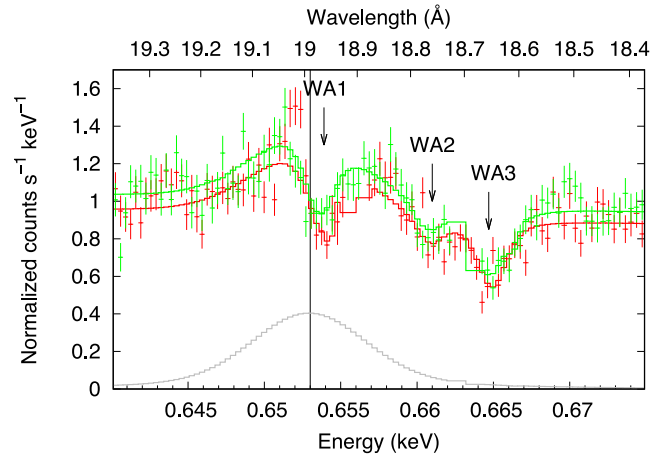


Figure 1. The O VIII Lyman α emission line and three absorption lines fitted with Gaussians. The red/green lines show the first order of RGS1/RGS2 spectra, respectively. The grey Gaussian shows the emission line. The central energy of the emission line, which has no velocity in the active galactic nucleus frame, is shown by the vertical line, and those of the absorption lines are shown by the arrows.

et al. 2007). `pexmon` is the model combining `pexrav` (Magdziarz & Zdziarski 1995) with self-consistently generated Fe and Ni lines, thus we can constrain the normalization of the reflection component from strength of the Fe K α line. When we assume that `pexmon` is at rest in the frame of NGC 4051, some residual is seen. Therefore we set the velocity of `pexmon` free to find that the velocity is -1800^{+500}_{-400} km s⁻¹. The column density of the galactic absorption towards this object is $(1.3 \pm 0.1) \times 10^{20}$ cm⁻² (Elvis, Wilkes & Lockman 1989), for which we added `tbabs` (Wilms, Allen & McCray 2000). As for the photoionized cross-section of `tbabs`, we used the one calculated by Balucinska-Church & McCammon (1992) and Yan, Sadeghpour & Dalgarno (1998). In order to fit the absorption features seen in the RGS spectra, we used a warm absorber model via `xstar` Version 2.2.1bn21 (Kallman et al. 2004), assuming the solar abundance and the photon index of the ionizing spectrum to be 2.0. We made a grid model by running `xstar` for different values of ξ and N_H ; the $\log \xi$ values were from 0.1 to 5 erg cm s⁻¹, and the N_H values were from 5×10^{20} to 5×10^{24} cm⁻². Fig. 1 shows the O VIII spectral shape, which has an emission line and three absorption lines. We fitted the spectral shape with a phenomenological model with power law, one positive Gaussian and three negative Gaussians. All of three negative Gaussians, shown by the arrows in Fig. 1, are blueshifted; their velocities are -600^{+90}_{-50} , -4040^{+70}_{-100} and -5780 ± 80 km s⁻¹. This shows that at least three independent warm absorbers are necessary to explain the observed absorption lines. We call these warm absorbers as WA1, WA2 and WA3, which have different ionization statuses and blueshifts. Emission lines, including radiative recombination continua (RRC), are also seen in the energy spectra, which are also observed by Nucita et al. (2010). We added positive Gaussians to explain these emission features. Table 2 shows a list of the emission lines.

We simultaneously fitted all the spectra with the following model:

$$F = \text{tbabs} \times \{(\text{diskbb} + \text{cutoffpl}) \times \text{WA1} \times \text{WA2} \times \text{WA3} + \text{pexmon} + \text{emission lines}\}, \quad (1)$$

and found that this model can almost fully explain the spectra, except two absorption lines. The O v 0.554 keV absorption line remains in the spectra, thus we added an additional narrow negative Gaussian. In addition, depth of the N VII 0.500 keV absorption line

Table 2. Identification of the observed emission lines; theoretically expected centroid energy (E_{exp}), observed ones (E_{obs}) and observed equivalent width (EW) are indicated.

Line	E_{exp}^a	E_{obs}	EW
N vi (f)	0.420 keV	0.419 keV	0.7 eV
O vii (f)	0.560 keV	0.560 keV	3.2 eV
O vii (i)	0.569 keV	0.568 keV	1.0 eV
O vii (r)	0.574 keV	0.573 keV	2.0 eV
O viii Ly α	0.654 keV	0.653 keV	8.3 eV
Fe xvii 3s-2p	0.726 keV	0.726 keV	2.2 eV
Ne ix (f)	0.905 keV	0.903 keV	4.0 eV
Ne ix (i)	0.915 keV	0.912 keV	0.7 eV
RRC of C vi	0.490 keV	0.492 keV	0.5 eV
RRC of O vii	0.739 keV	0.735 keV	2.6 eV

^aFrom the CHIANTI data base (Dere et al. 2001).

seems to be overestimated in the model, thus we added a positive Gaussian, which might be a real emission line (Nucita et al. 2010). Figs 2, 3 and Table 3 show the fitting results. The reduced chi square (χ_v^2) is 1.52 for the degree of freedom (dof) of 8928. Fig. 4 shows the absorption features created by WA1, WA2 and WA3. We can see that WA1 creates a deep Fe-L unresolved transition array (UTA) feature at ≈ 0.8 keV (Behar, Sako & Kahn 2001).

3.2 rms spectra

3.2.1 Calculation of rms

In order to evaluate spectral variability, we calculated root mean square (rms) of the data. We adopt the fractional variability

amplitude (F_{var}) and the point-to-point fractional variability (F_{pp}), which are defined as

$$F_{\text{var}} = \frac{1}{\langle X \rangle} \sqrt{S^2 - \langle \sigma_{\text{err}}^2 \rangle}, \quad (2)$$

and

$$F_{\text{pp}} = \frac{1}{\langle X \rangle} \sqrt{\frac{1}{2(N-1)} \sum_{i=1}^{N-1} (X_{i+1} - X_i)^2 - \langle \sigma_{\text{err}}^2 \rangle}, \quad (3)$$

where X_i is the count for the i th of N bins, $\langle X \rangle$ is the mean count rate, S^2 is the variance of the light curve and $\langle \sigma_{\text{err}}^2 \rangle$ is the mean error squared (Edelson et al. 2002). The error on $F_{\text{var,pp}}$ is given as

$$\sigma_{F_{\text{var,pp}}} = \frac{1}{F_{\text{var,pp}}} \sqrt{\frac{1}{2N} \frac{S^2}{\langle X \rangle^2}}. \quad (4)$$

F_{var} shows the long-time-scale variability across the whole observation period ($\sim 10^5$ s in this data set), whereas F_{pp} extracts the variability at a given time-scale. See the appendix of Edelson et al. (2002) how to derive these equations.

We calculated F_{var} and F_{pp} using all the 15 observations. When calculating rms of the RGS data, we used only the first order of the 0.4–1.6 keV energy band to maximize photon statistics. Fig. 5 shows the F_{var} spectra with a time bin-width of 5000 s for the entire observation period ($N = 111$). We can see several important features in the rms spectra. First, the bin at ≈ 6.4 keV drops, which is considered as due to the fluorescent Fe-K line that has little variability (Ponti et al. 2006; Terashima et al. 2009). The rms spectrum has a peak in the soft energy band, and the value gradually decreases towards higher energies, which is common in several Seyfert 1 galaxies (Terashima et al. 2009 and referenced therein). We can see more detailed features in the RGS data; in particular, it has a strong peak at 0.8 keV, and sharp drops at 0.55 and 0.9 keV.

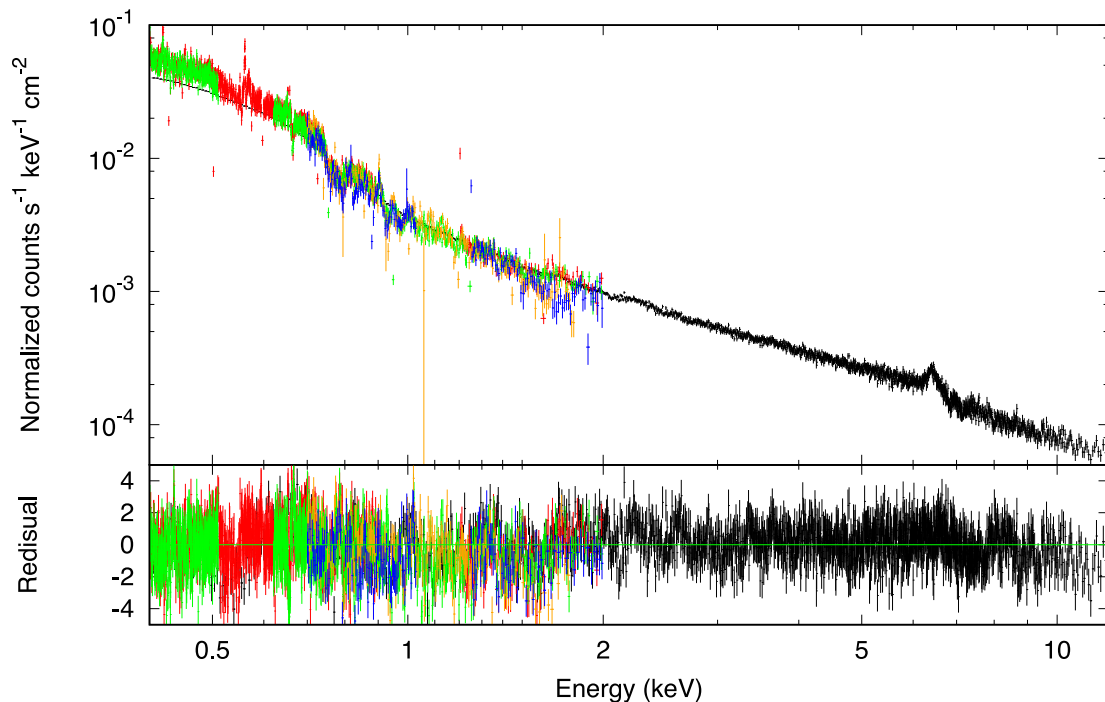


Figure 2. Spectral fitting of NGC 4051. The black, red, green, orange and blue show the EPIC-pn, first order of RGS1, first order of RGS2, second order of RGS1 and second order of RGS 2 spectra, respectively. The black line shows the model. The upper panel shows count plots, removing effect of effective areas ('setplot area' in XSPEC), and the lower panel shows the residuals (χ), which mean (data–model)/error. The shown data are more binned than those used in the spectral fitting for clarity.

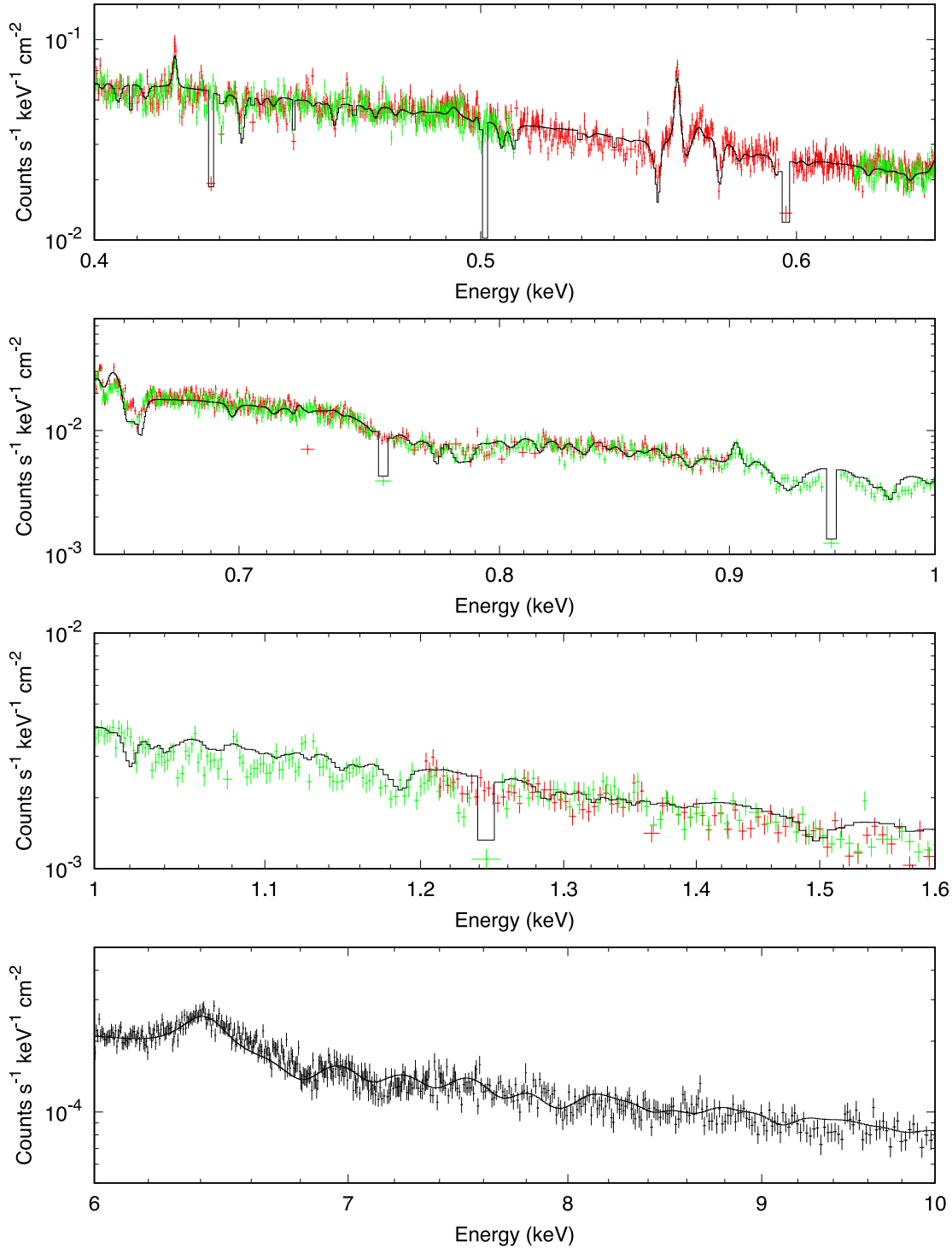


Figure 3. Enlargement of the upper panel of Fig. 2 in order to clarify the emission/absorption line features. The model lines are those of RGS1 (0.4–0.65 keV), RGS2 (0.65–1.6 keV) and EPIC-pn (6–10 keV).

3.2.2 Absorption/Emission features

First, we focus on the rms peak at $\simeq 0.8$ keV. This energy corresponds to that of the Fe-L UTA. When depth of the absorption feature varies, such an rms peak is created. When only N_{H} of the absorber varies, rms is calculated to be

$$F_{\text{var}} = (N_{\text{H}})_{\text{var}} \cdot \frac{\sigma(E)\langle N_{\text{H}} \rangle}{1 - \sigma(E)\langle N_{\text{H}} \rangle}, \quad (5)$$

where $\sigma(E)$ is the photoionized cross-section, $\langle N_{\text{H}} \rangle$ is the average value of N_{H} and $(N_{\text{H}})_{\text{var}}$ is the variability amplitude of N_{H} (Appendix A1). In the optically thin regime, variation of N_{H} is equivalent to variation of the partial covering fraction as follows:

$$\begin{aligned} W &= \exp[-\sigma N_{\text{H}}] \\ &\simeq 1 - \sigma N_{\text{H}} \\ &= 1 - \alpha \sigma N_{\text{H}}^{\text{fixed}} \end{aligned}$$

Table 3. Parameters of spectral fitting.

tbabs	N_{H} (cm^{-2})	1.3×10^{20} (fix) ^a
diskbb	T_{in} (eV)	155.9 ± 0.6
	Norm. ^b	2610 ± 40
cutoffpl	Γ	1.581 ± 0.006
	E_{c} (keV)	500 (fix)
	Norm. ^c	$(3.42 \pm 0.02) \times 10^{-3}$
pexmon	$\Omega/2\pi$	0.49 ± 0.07
	Inclination	60° (fix)
	v (km s^{-1})	-1800_{-400}^{+500}
WA1	N_{H}	$(2.46 \pm 0.07) \times 10^{21}$
	$\log \xi$	1.469 ± 0.009
	v (km s^{-1})	-650 ± 20
WA2	N_{H}	$(8.2_{-0.3}^{+0.4}) \times 10^{21}$
	$\log \xi$	2.512 ± 0.013
	v (km s^{-1})	-4060 ± 60
WA3	N_{H}	$(7.1_{-0.9}^{+1.1}) \times 10^{23}$
	$\log \xi$	$3.383_{-0.006}^{+0.011}$
	v (km s^{-1})	-6120 ± 20

^aFrom Elvis et al. (1989).

^b $(\frac{r_{\text{in}}/\text{km}}{D/10\text{kpc}})^2 \cos i$, where r_{in} is the inner radius, D is the distance and i is the inclination angle.

^cPhotons $\text{keV}^{-1} \text{cm}^{-2} \text{s}^{-1}$ at 1 keV.

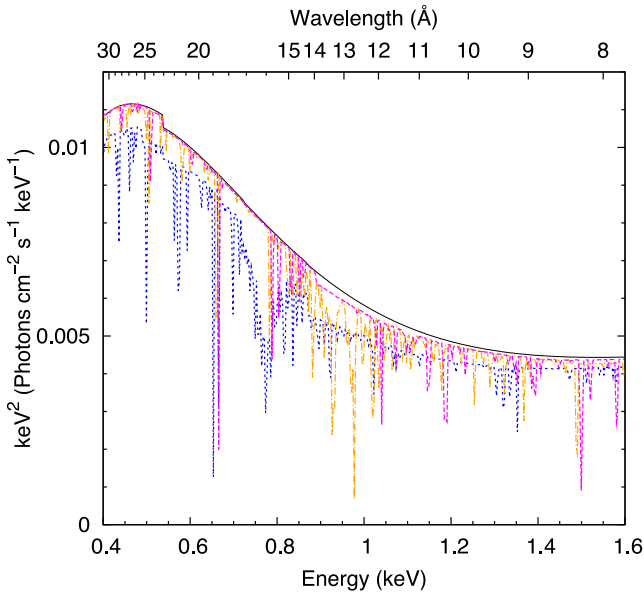


Figure 4. Model spectra of three warm absorbers. The black line shows the continuum ($\text{tbabs} \times (\text{diskbb} + \text{cutoffpl})$), and the blue dotted, orange dot-dashed and magenta dashed lines show the continuum with WA1, WA2 and WA3, respectively.

$$\begin{aligned}
 &= 1 - \alpha + \alpha (1 - \sigma N_{\text{H}}^{\text{fixed}}) \\
 &\simeq 1 - \alpha + \alpha \exp[-\sigma N_{\text{H}}^{\text{fixed}}] \\
 &= 1 - \alpha + \alpha W^{\text{fixed}},
 \end{aligned} \tag{6}$$

where α is the partial covering fraction and $N_{\text{H}}^{\text{fixed}}$ is the full-covering column density (see equation 5 of Mizumoto, Ebisawa & Sameshima 2014). When the partial covering fraction varies, rms is calculated to be

$$F_{\text{var}} = (\alpha)_{\text{var}} \cdot \frac{(1 - \exp[-\sigma(E)N_{\text{H}}^{\text{fixed}}]) \langle \alpha \rangle}{1 - (1 - \exp[-\sigma(E)N_{\text{H}}^{\text{fixed}}]) \langle \alpha \rangle} \tag{7}$$

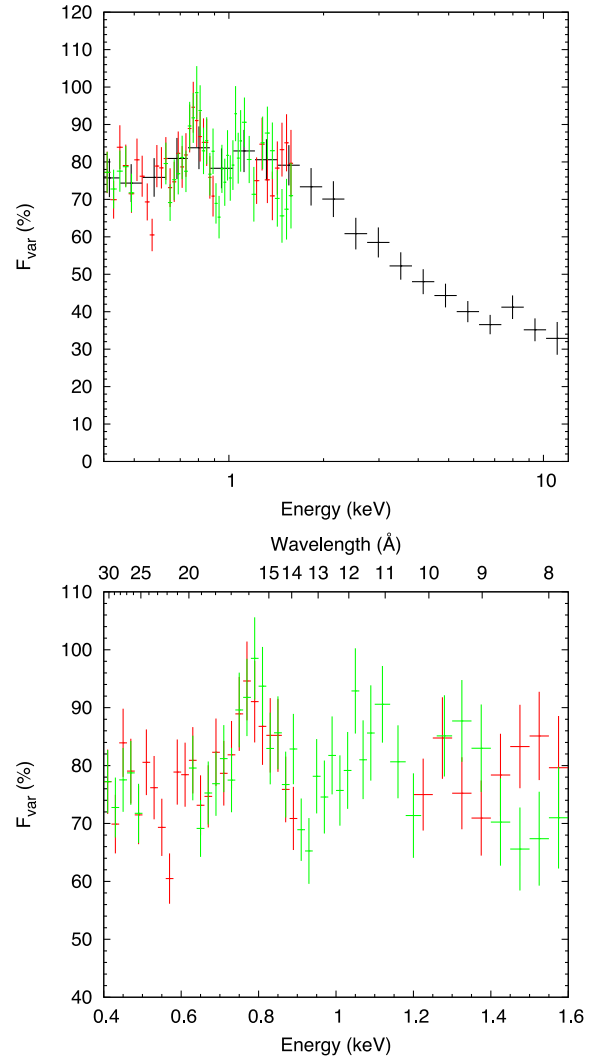


Figure 5. rms spectra of EPIC-pn (black) and first order of RGS1/2 (red/green), respectively, with a bin-width of 5000 s. The lower panel is an enlargement of the upper panel (only RGS data).

(Appendix A2). Equations (5) and (7) are mathematically equivalent; both equations monotonically increase with $\sigma(E)$, which means that rms peaks appear at the energy band where the absorption features are deeper than the adjacent bands (see fig. 10 of Yamasaki et al. 2016).

We calculated simulated rms spectra in order to illustrate effects of the warm absorber variations in the rms spectra. The method is as follows. (1) We set a range of the variable column densities as $[(N_{\text{H},k} - \Delta N_{\text{H},k} : N_{\text{H},k}) + \Delta N_{\text{H},k}]$ for each WAK ($k = 1, 2, 3$), or, equivalently a range of the variable partial covering fractions as $[(\alpha_k) - \Delta \alpha_k : \langle \alpha_k \rangle + \Delta \alpha_k]$. (2) We substituted $N_{\text{H},k}$ or α_k of the k th absorber random values within the covering range, and created simulated energy spectra using `fakeit` command in `XSPEC`. (3) We repeated the procedure 100 times and got 100 simulated energy spectra for each k . (4) We calculated the simulated rms spectra from the 100 simulated energy spectra.

Fig. 6 shows the simulated rms spectra. The blue/orange/magenta lines show the rms spectra when the parameter of WA1/WA2/WA3 varies, respectively, at the same amounts. The black line is the sum of them. We set $\Delta N_{\text{H},k}/N_{\text{H},k}$ or $\Delta \alpha_k/\langle \alpha_k \rangle$ as 100 per cent, i.e. $(N_{\text{H}})_{\text{var}} = (\alpha)_{\text{var}} = 100/\sqrt{3} = 57.7$ per cent, for each k

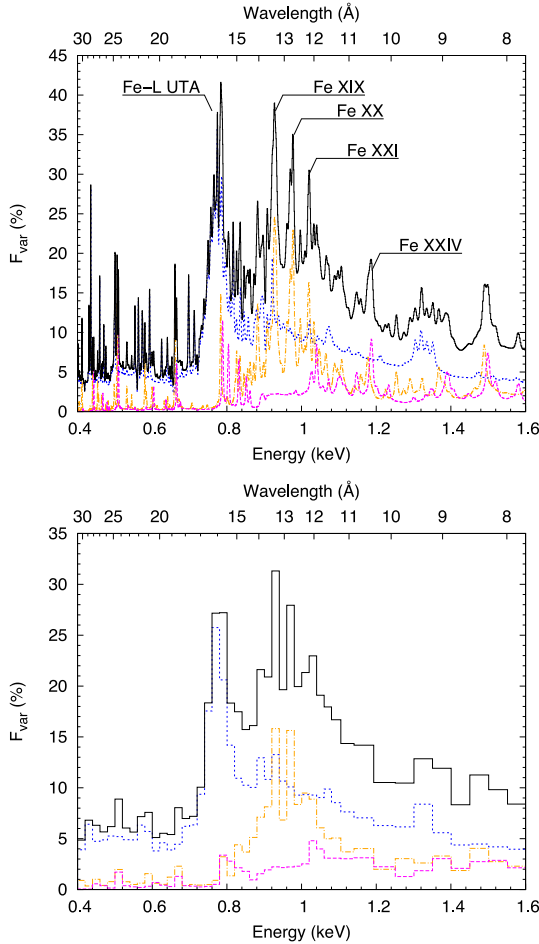


Figure 6. Simulated rms spectra when either column densities or partial covering fractions of the warm absorbers vary. The blue dotted, orange dot-dashed and magenta dashed lines show the effect of WA1, WA2 and WA3, respectively, and the black line is the sum of them. The lower panel is the same as the upper one, but binned with the bin-width of Fig. 5 bottom.

(Appendix A1). We can see that the rms peak at ~ 0.8 keV is explained by the Fe-L UTA feature of WA1. In addition, other peaks are seen at the 0.9–1.0 keV band from WA2 and WA3.

Next, we focus on the rms dips at 0.55 and 0.9 keV. When emission lines have little variations whereas the entire spectrum varies, the variability amplitude at the lines are less than those of the adjacent ranges. When the adjacent range varies with a variability amplitude of $F_{\text{var,adj}}$, the variability amplitude of the non-variable emission lines ($F_{\text{var,line}}$) is calculated as

$$F_{\text{var,line}} = F_{\text{var,adj}} \cdot \frac{1}{1+x}, \quad (8)$$

where x is the intensity ratio of the line to the adjacent continuum (Appendix A3). This means that rms spectra show drops at the non-variable emission lines. In order to evaluate effect of the emission lines, we simulated the rms spectra, where only normalization of the continuum is varied. Fig. 7 shows the effect of the non-variable lines, that is $1/(1+x)$ of equation (8). We can see that these lines appear as significant dips in the rms spectra, if only the continuum is variable.

We compared the observed F_{var} spectra with the simulated ones. If all the warm absorbers had the same variability amplitudes, a significant peak at the 0.9–1.0 keV band from WA2 and WA3 would

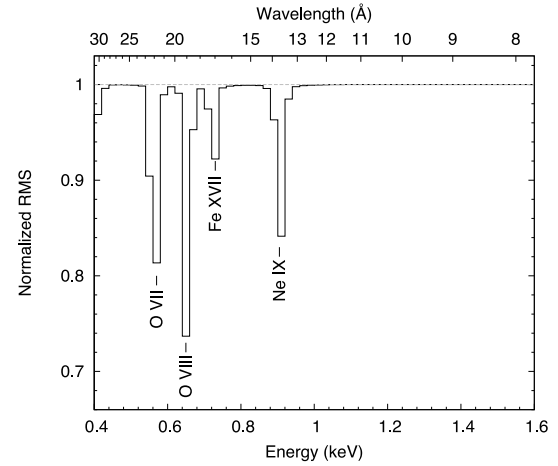


Figure 7. Simulated rms spectra when emission lines are not variable.

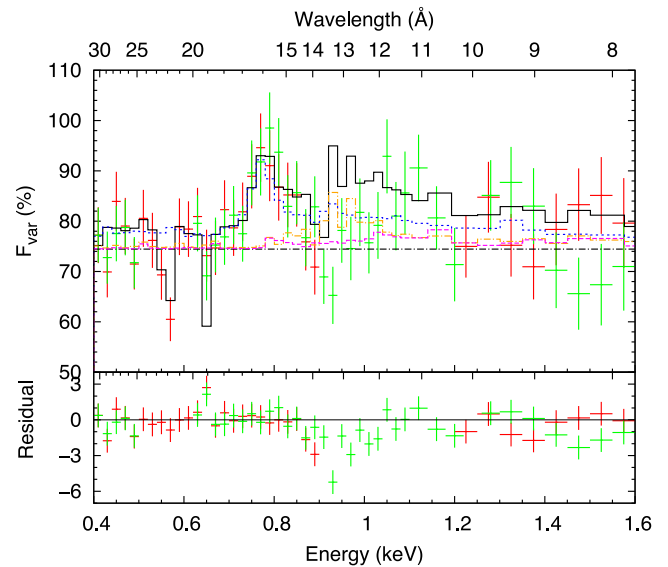


Figure 8. Fitting of the F_{var} spectra with the simulated ones when all the warm absorbers have the same variability amplitude. The red/green bins show the data of first order of RGS1/RGS2. The types of the model lines are same as Fig. 6, and the black dashed line shows the continuum level.

be seen (Fig. 8). However, the F_{var} spectra have no peak at the energy band, thus we propose that only WA1 has a large variability, whereas WA2 and WA3 have little variability.

Fig. 9 and Table 4 show the fitting results, where parameters are the fractional variability of three warm absorbers and the continuum normalization. All the features in the F_{var} spectra are explained by the model fitting ($\chi^2_{\nu} = 0.99$ for dof = 68). In particular, the rms dips at $\simeq 0.55$ and $\simeq 0.9$ keV are explained well by the O VII (f) and Ne IX (f) emission lines. WA1 varies significantly as much as 42 ± 8 per cent, whereas WA2 varies little (< 5 per cent), and variation of WA3 cannot be constrained (< 49 per cent). We notice that the continuum level shows a large variability, which means that the observed soft X-ray flux varies due to other mechanisms.

Fig. 10 and Table 5 show the fitting results of the F_{pp} spectra. The structure of the F_{pp} spectra are similar to that of the F_{var} spectra. WA1 shows large variability in all the examined time-scales. In particular, the variability is largest at the time-scale of $\sim 10\,000$ s.

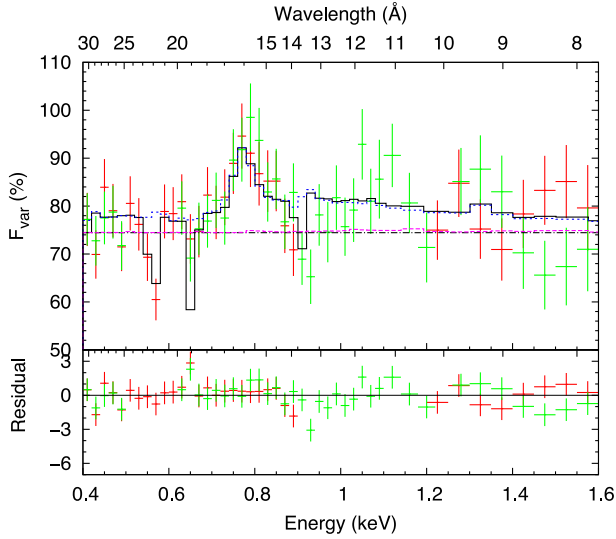


Figure 9. Same as Fig. 8, but the variability amplitude of each warm absorber is set to be free.

Table 4. Parameters of the F_{var} spectral fitting.

	Fractional variability amplitude
WA1	42 ± 8 per cent
WA2	0^{+5} per cent
WA3	9 ± 40 per cent
Continuum	74.5 ± 1.3 per cent
χ^2_{ν} (dof)	0.99 (68)

On the other hand, WA2 and WA3 show little variability in all the time-scales.

3.3 Spectral variations in the whole X-ray band

We have found that the observed soft X-ray flux and the parameter of WA1 show large variations in the previous subsection. In order to investigate time variations of the parameters, we divided the RGS spectra with a time bin-width of 3000 s, created 172 spectra and fitted them with the following model:

$$F(t) = \text{tbabs} \times \{(\text{diskbb} + \text{cutoffpl}) \times C(t) \times \text{WA1}(t) \times \text{WA2} \times \text{WA3} + \text{pexmon} + \text{emission lines}\}, \quad (9)$$

where $C(t)$ shows variation of the continuum normalization or variation of the observed soft X-ray flux. The variable parameters are only $C(t)$ and $N_{\text{H},1}(t)$, where $\text{WA1}(t) = \exp[-\sigma_{\text{T}} N_{\text{H},1}(t)]$. Variation of $N_{\text{H},1}(t)$ is mathematically equivalent to variation of partial covering fraction of WA1, as shown in equation (6). All the other parameters are fixed at those in the best-fit of the time averaged spectrum (Table 3). Fig. 11 shows the time variations of $N_{\text{H},1}(t)$ and $C(t)$. We found that both the $N_{\text{H},1}$ (or partial covering fraction of WA1) and the observed soft X-ray flux have large variations. In particular, in the observational sequences of 3, 5, 6, 7 and 8 (marked with the green rectangles in Fig. 11), these parameters are clearly anticorrelated, whereas in the other sequences they are not obviously correlated. In Obs 3, 5, 6, 7 and 8, no lags are seen between the two parameters at a time-scale of 3000 s.

4 DISCUSSION

4.1 Origin of the observed flux/spectral variation

In order to explain X-ray variation of NGC 4051, several models have been proposed. Kunieda et al. (1992) proposed a ‘blob model’, where Compton-thick blobs move around the X-ray emission region, and observed X-ray flux/spectral variations occur due to change of the number of blobs in the line of sight. Similarly, partial covering models have been investigated in NGC 4051, where the observed flux/spectral variations mainly (especially in the soft X-ray energy band) result from variable partial covering fraction of the intervening absorbers (e.g. Pounds et al. 2004; Haba et al. 2008; Terashima et al. 2009; Lobban et al. 2011; Iso et al. 2016). Meanwhile, some authors argue that ionization states of the absorbers vary (Krongold et al. 2007; Steenbrugge et al. 2009; Silva, Uttley & Costantini 2016; see Section 4.4). Here, we assume that the Compton-thick blobs responsible for the variation of the observed soft X-ray flux exist around the central X-ray emission region, in addition to the ionized blobs (=WA1) responsible for the variable absorption feature. In this manner, we introduce two partial covering layers, one is due to the Compton-thick absorbers and the other is due to WA1. Indeed, in equation (9), we assume that

$$C(t) = 1 - \alpha(t) \simeq 1 - \alpha(t) + \alpha(t)W_{\text{thick}}, \quad (\text{when } E < 2 \text{ keV}), \quad (10)$$

where W_{thick} indicates the Compton-thick absorber, and

$$\text{WA1}(t) \simeq 1 - \beta(t) + \beta(t)\text{WA1}, \quad (11)$$

following equation (6). $\alpha(t)$ and $\beta(t)$ show variable partial covering fractions of the Compton-thick absorbers and WA1, respectively. Under these assumptions, equation (9) can be written as

$$F = \text{tbabs} \times \{[(1 - \alpha(t)) + \alpha(t)W_{\text{thick}}] \times (\text{diskbb} + \text{cutoffpl}) \times [(1 - \beta(t)) + \beta(t)\text{WA1}] \times \text{WA2} \times \text{WA3} + (\text{pexmon} + \text{emission lines})\}. \quad (12)$$

We suppose that such a correlation exists between $\alpha(t)$ and $\beta(t)$, that, when the partial covering fractions increase, the observed soft X-ray flux gets weaker due to the Compton-thick absorbers, and the Fe-L absorption feature gets deeper due to WA1. When the partial covering fractions decrease, vice versa.

When the partial covering fraction of the Compton-thick blobs [= $\alpha(t)$] is variable, observed X-ray flux in the EPIC energy band should also vary. We created intensity-sliced spectra of the EPIC data for each observational sequence (3, 5, 6, 7 and 8) as follows. (1) We created light curves with a bin-width of 256 s in the 0.4–12.0 keV band. (2) We calculated all counts in each observational sequence, and determined the four intensity ranges that contain almost the same counts. (3) From the four time-periods corresponding to the different flux levels, we created the four intensity-sliced energy spectra in each observational sequence. The fitting model is equation (12). We fixed $N_{\text{H},\text{thick}}$ as $1.5 \times 10^{24} \text{ cm}^{-2}$, which is inverse of Thomson scattering cross-section, and ξ as $10^{0.1}$, which means that W_{thick} is cold. The velocity is fixed as $v = -660 \text{ km s}^{-1}$, which is consistent with WA1. The fittings were performed for each observational sequence. We allowed the parameters of the continuum to vary among different observational sequences, but not to vary within a single sequence. In each sequence, only α and β were allowed to be free. Namely, we assumed that, during each sequence, the intrinsic source luminosity in the fitting band (0.4–10 keV) is not

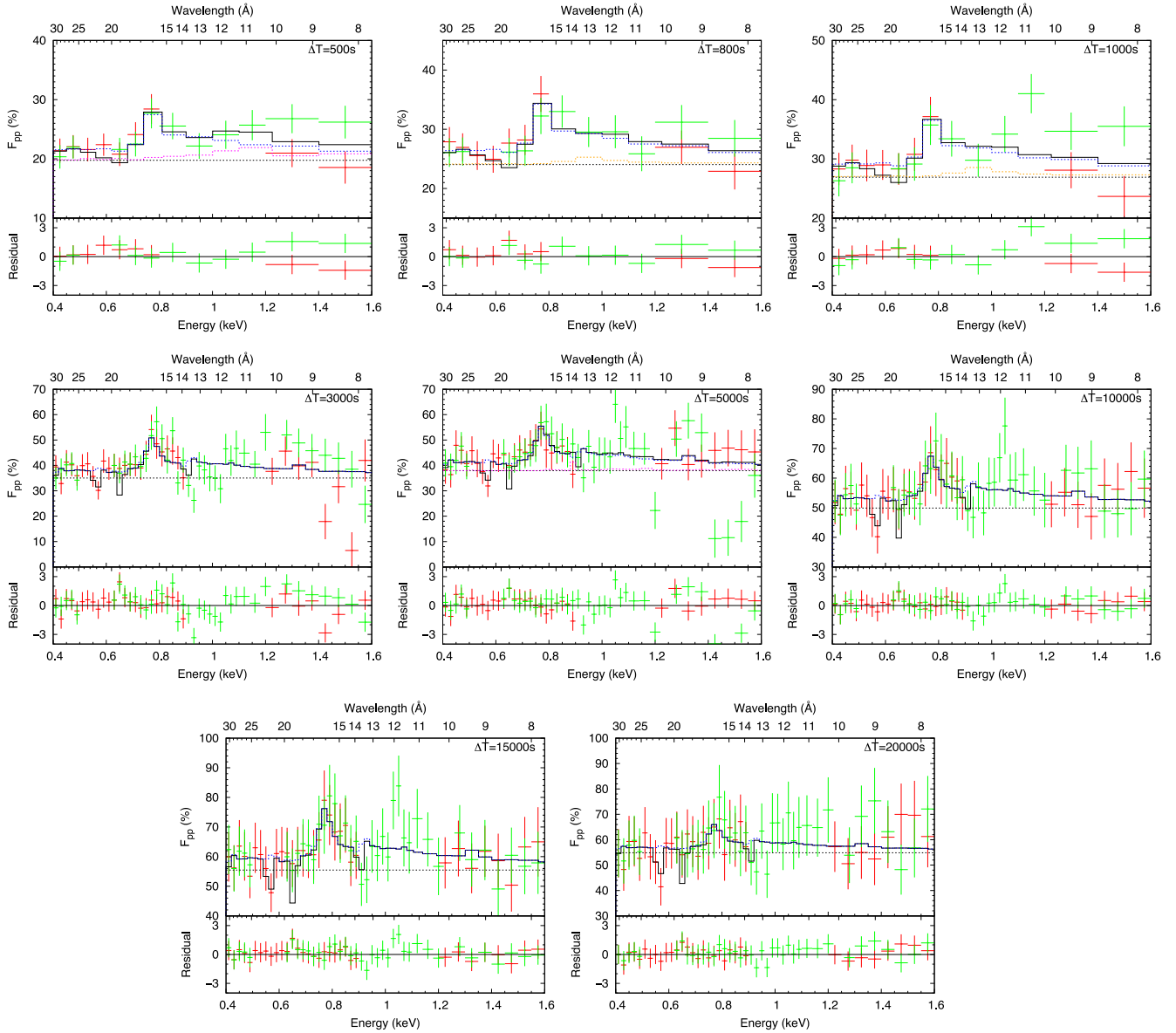


Figure 10. Fitting of the F_{pp} spectra with absorption/emission models at various time-scales where variability amplitude of each warm absorber and the continuum level are free.

variable and the observed flux variation is only due to occultation by the partial covering blobs.

Fig. 12 shows the fitting results of Obs 5. We can explain the spectral variability in the whole 0.4–12.0 keV band with variations of only the two partial covering fractions ($\chi^2_{\nu} \simeq 1.1$). The fitting results of the other sequences are also reasonable ($\chi^2_{\nu} < 1.3$). Fig. 13 shows correlation of the two partial covering fractions: The two parameters are clearly correlated, as expected. The red line shows the best-fitting linear function with the boundary condition going through the origin ($\alpha = \beta = 0$), and the yellow area shows the error region; we see that $\alpha = \beta$ holds. The column density ($N_{\text{H}}^{\text{fixed}}$) of WA1 is $(6.4^{+1.3}_{-2.1}) \times 10^{21} \text{ cm}^{-2}$, and the average α is ~ 0.4 .

In Obs 3, 5, 6, 7 and 8, the observed spectral/flux variability of NGC 4051 can be explained only by change of the partial covering fraction, whereas the intrinsic luminosity is not variable. On the other hand, in the other observational sequences, we cannot see clear anticorrelation between the observed flux and the partial covering fraction, which presumably suggests that not only the partial

covering fraction but also the intrinsic luminosity are variable. For example, in Obs 2, whereas the absorbers have little variations, the intrinsic luminosity variability is large, thus we can see significant variability of the observed flux. Table 6 shows variability of the partial covering fractions and the intrinsic luminosity for each observational period. We can see the anticorrelation when the partial covering fractions vary and the intrinsic luminosity do not vary (in the situation B in Table 6). Time-scale of the intrinsic luminosity variation is $\lesssim 6000 \text{ s}$ ($= 2$ bins in Fig. 11), which is similar to that of the partial covering fraction.

Consequently, the spectral components and their variability are explained by the following equation:

$$\begin{aligned}
 F = & \text{tbabs} \times \{[(1 - \alpha(t)) + \alpha(t)W_{\text{thick}}] \\
 & \times (\text{diskbb} + \text{cutoffpl}(t)) \times [(1 - \alpha(t)) + \alpha(t)WA1] \\
 & \times WA2 \times WA3 + (\text{pexmon} + \text{emission lines})\}. \quad (13)
 \end{aligned}$$

Table 5. Parameters of F_{pp} spectral fitting.

	500 s	800 s	1000 s	3000 s	5000 s	10 000 s	15 000 s	20 000 s
WA1	22 ± 6 per cent 0 ⁺¹¹ per cent	30 ± 7 per cent 7 ± 18 per cent	28 ± 8 per cent 9 ± 20 per cent	37 ± 7 per cent 0 ⁺⁴ per cent	41 ± 8 per cent 0 ⁺⁹ per cent	41 ± 10 per cent 0 ⁺¹⁶ per cent	49 ± 11 per cent 0 ⁺¹⁷ per cent	26 ± 13 per cent 0 ⁺²¹ per cent
WA2	26 ± 28 per cent	0 ⁺²⁹ per cent	0 ⁺⁹⁵ per cent	0 ⁺³³ per cent	10 ± 40 per cent	0 ⁺¹⁴ per cent	0 ⁺¹¹⁶ per cent	0 ⁺¹⁴¹ per cent
WA3	19.8 ± 0.8 per cent	24.0 ± 1.0 per cent	26.9 ± 1.1 per cent	35.0 ± 1.0 per cent	37.9 ± 1.2 per cent	49.9 ± 1.5 per cent	55.5 ± 1.7 per cent	55 ± 2 per cent
Constant	0.62 (16)	0.49 (16)	1.39 (16)	1.50 (68)	1.44 (68)	0.51 (68)	0.46 (68)	0.44 (68)
χ^2_v (dof)								

Note. The fractional variability amplitude is shown.

4.2 Variable double partial covering model

We have shown that ‘double partial covering’ with the same partial covering fractions can explain the observed spectral/flux variability of NGC 4051 in the 0.4–10 keV. Indeed, equation (13) is equivalent to the ‘variable double partial covering (VDPC) model’, which was originally proposed for MCG–6–30–15 by Miyakawa, Ebisawa & Inoue (2012), refined by Mizumoto et al. (2014), and confirmed for various NLS1s by Iso et al. (2016) and Yamasaki et al. (2016). In the VDPC model, the commonality of the two partial covering fractions is explained by double-layer absorbers, and the spectral variations of NLS1s are explained by the partial covering fraction of the double-layer absorbers, as well as independent variation of the continuum normalization. Our results on NGC 4051 confirm validity of the VDPC model. This double-layer absorber is very similar to the cometary one proposed in Maiolino et al. (2010).

4.3 Physical parameters of the warm absorber outflows

We have found that WA1 shows large variability at time-scales of ~10 ks. Assuming that the warm absorber follows Kepler motion at the distance of r from the black hole, we have

$$\frac{r}{R_s} = 2 \times 10^3 \left(\frac{\Delta T}{10^4 \text{ [s]}} \right)^2 \left(\frac{D}{10 R_s} \right)^{-2} \left(\frac{M_{\text{BH}}}{1.7 \times 10^6 M_\odot} \right)^{-2}, \quad (14)$$

where R_s is the Schwarzschild radius, ΔT is the time-scale at which the absorber passes in front of the X-ray emission region, D is the diameter of the X-ray emission region and M_{BH} is the black hole mass. WA1 shows the largest variability at $\Delta T = 10^4$ s, which corresponds to $r \sim 10^3 R_s$, whereas variability is seen at all the examined time-scales. WA1 and W_{thick} share the same blobs, thus the location of WA1 and W_{thick} is identical. When the location of the blobs is $\sim 10^3 R_s$, the number density and the thickness of W_{thick} /WA1 are calculated as $2 \times 10^{12} \text{ cm}^{-3}/7 \times 10^{10} \text{ cm}^{-3}$ and $1 \times 10^{12} \text{ cm}/1 \times 10^{11} \text{ cm}$, respectively. This shows that the blob is composed of a cold and dense core, and a warm and thin layer.

We cannot strongly constrain location of WA3 from the spectral variation. From the constraint that $\Delta r \leq r$, WA3 presumably locates at $r \leq 3 \times 10^{14} \text{ cm} = 6 \times 10^2 R_s$, and $n \geq 2 \times 10^9 \text{ cm}^{-3}$.

WA2 shows little variability in both F_{var} and F_{pp} spectra, therefore we assume that WA2 extends uniformly in the line of sight. The number density of WA1 and WA3 are $7 \times 10^{10} \text{ cm}^{-3}$ and $\geq 2 \times 10^9 \text{ cm}^{-3}$, therefore we assume that the number density of WA2 is an order of $\sim 10^{10} \text{ cm}^{-3}$. If so, the parameters WA2 are estimated as $r \sim 4 \times 10^{14} \text{ cm} = 8 \times 10^2 R_s$ and $\Delta r \sim 9 \times 10^{11} \text{ cm}$. Table 7 shows the estimated parameters of the absorbers.

4.4 Comments on an alternative scenario

Some authors propose that observed spectral variation in NGC 4051 is due to variation of ionization degree, whereas other parameters of the warm absorbers are less variable (Krongold et al. 2007; Steenbrugge et al. 2009; Silva et al. 2016). In this scenario, the variable X-ray luminosity explains the ionization degree variation, such that the absorber is more ionized and transparent when the intrinsic luminosity is higher. In order to investigate the effect of variation of the ionization degree, we calculate the rms spectrum when the ionization degree of WA1 is variable within $1 \leq \log \xi \leq 2$ by one order of magnitude (Krongold et al. 2007). Fig. 14 shows the simulated rms spectra and the fitting results. Whereas the centroid

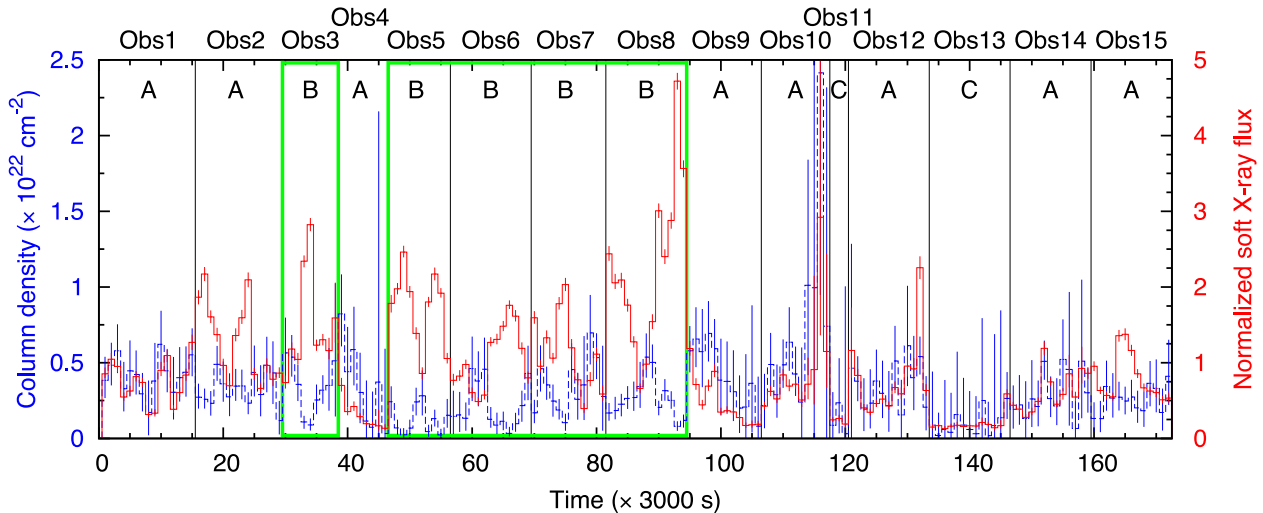


Figure 11. Variations of the column density of WA1 [= $N_{\text{H},1}(t)$; blue dashed] and the normalized flux observed in the soft energy band [= $C(t)$; red solid]. The time bin-width is 3000 s. The partial covering fraction is calculated as $N_{\text{H}}/N_{\text{H}}^{\text{fixed}}$. In Obs 3 and 5 to 8 (surrounded by green lines), anticorrelation was observed between the column density (partial covering fraction) and the observed soft X-ray flux. See the caption of Table 6 for explanation of the labels A, B and C.

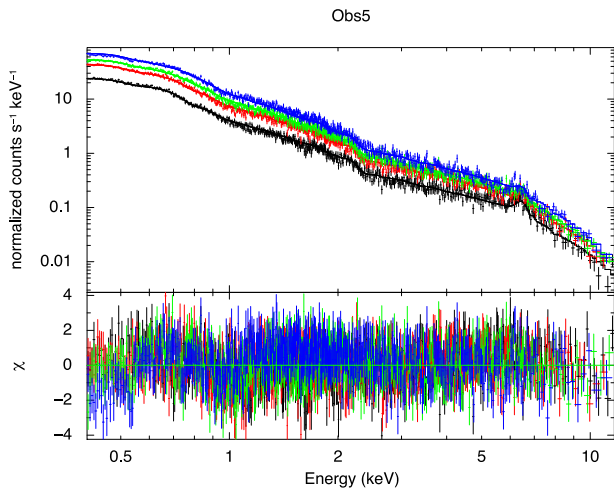


Figure 12. Simultaneous fitting of the intensity-sliced spectra in Obs 5. Only the partial covering fraction of W_{thick} and the column density/the partial covering fraction of WA1 are variable.

energy of the peak is slightly lower than that when the N_{H}/α varies, the fitting is reasonable ($\chi^2_{\nu} = 1.49$ for dof = 71).

Our observational results clearly show that highly ionized absorbers (WA2 and WA3) have little variability, whereas WA1 has large variability. If number densities of WA2 and WA3 are sufficiently small ($n \sim 10^7 \text{ cm}^{-3}$), equilibrium time-scales of the absorbers are so large that we may not see ionization degree variability (Nicastrò et al. 1999; Silva et al. 2016), and WA2 and WA3 are calculated to locate far from the central black hole ($r \sim 10^{17} \text{ cm}$). However, this scenario is against the condition that the number density of WA3 is $\geq 2 \times 10^9 \text{ cm}^{-3}$ and the distance is $\leq 3 \times 10^{14} \text{ cm}$ (see Section 4.3). Furthermore, occasional independence of the observed X-ray flux and the opacity of WA1 (Fig. 11 and Table 6) has yet to be explained, since intrinsic luminosity variation should always affect ionization state of the absorber.

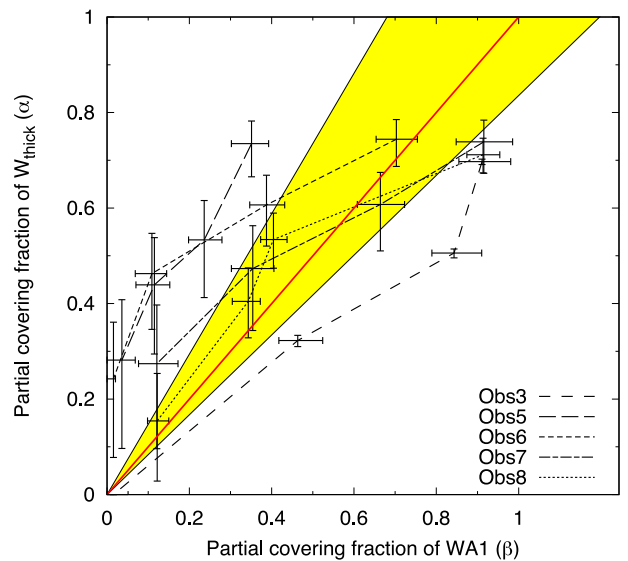


Figure 13. Correlation of the partial covering fraction of W_{thick} and WA1 when $N_{\text{H}}^{\text{fixed}}$ of WA1 is $6.4 \times 10^{21} \text{ cm}^{-2}$. The red line shows the best-fitting, and the yellow area shows the error range.

4.5 Nature of the warm absorber outflows

From the frequency- and energy-dependent time-lags, Miller et al. (2010) proposes that the absorbing/reflecting clouds in NGC 4051 extend to a distance of $\simeq 1.5 \times 10^{14} \text{ cm}$ with a covering fraction of $\gtrsim 0.44$. These physical parameters of the clouds are consistent with the partial covering blobs we found, although derived in totally different manners. In addition, Kaastra et al. (2014) propose that NGC 5548 has low-ionized outflowing obscurers at a location of $\sim 10^3 R_s$, which is also similar to our partial covering blobs. Moreover, similar clouds have been introduced in various NLS1s (see e.g. Miller, Turner & Reeves 2009; Iso et al. 2016). Thus the outflowing absorbing blobs may commonly exist in the NLS1s. The fluorescent Fe-K line of NGC 4051 is blueshifted at a velocity of -1800 km s^{-1} (see Section 3.1), which supports that the clouds

Table 6. Variability of the partial covering fractions and the intrinsic luminosity.

Obs.	Partial covering	Intrinsic	Observed variability ^a
1	×	○	A
2	×	○	A
3	○	×	B
4	○	○	A
5	○	×	B
6	○	×	B
7	○	×	B
8	○	×	B
9	○	○	A
10	○	○	A
11	×	×	C
12	×	○	A
13	×	×	C
14	×	○	A
15	×	○	A

^aA: the observed flux variability is mostly due to variation of the intrinsic luminosity. B: the observed flux variability is mostly due to variation of the partial covering fraction. C: the observed flux is hardly variable.

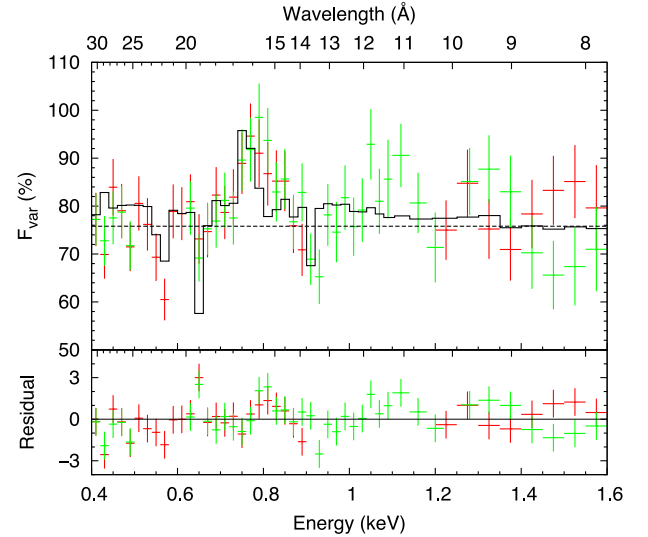
not only absorb but also reflect X-rays. Intensity of the reflection component is determined by the solid angle of the clouds, thus non-variability of the fluorescent Fe-K line means that the solid angle of the clouds is invariable. Those clouds in charge of the fluorescent line are out of the line of sight, and distributed over a wide solid angle. Whereas the clouds in the line of sight show instantaneous variation, solid angle of the clouds is presumably not significantly variable within each observation sequence.

WA2 and WA3 locate at $\lesssim 10^3 R_s$, close to the central X-ray source, thus the warm absorbers are presumably launched as disc winds, because other mechanisms such as thermal-driven winds require extremely high temperature in this situation (e.g. King et al. 2012). The line-driven disc wind, which is powered by radiation force due to spectral lines, is one of the plausible mechanism to produce warm absorber outflows (see e.g. Proga, Stone & Kallman 2000). Fig. 5 in Nomura et al. (2016) shows a simulation of the geometry of the line-driven disc wind with M_{BH} of $10^6 M_\odot$ and the Eddington ratio of 0.5, where the outflow velocity reaches $\sim 15000 \text{ km s}^{-1}$. Densities, ionization degrees and locations of WA2 and WA3 are consistent with their simulation. NGC 4051 is considered to have a low Eddington ratio ($\lesssim 0.1$; Czerny et al. 2001) than that assumed in Nomura et al. (2016), thus the outflow velocity would be slower; this is likely to explain the observed outflow velocities of WA2 and WA3. In this manner, we suggest that WA2 and WA3 originate in the line-driven disc winds.

Fig. 15 shows a schematic picture of NGC 4051. In summary, we have found that NGC 4051 has two types of the warm absorber outflows; one is the line-driven disc winds and the other is the double-layer blobs. The line-driven disc winds are launched within several hundred R_s , and extend uniformly in the line of sight, thus they

Table 7. Parameters of the absorbers.

		$n \text{ (cm}^{-3}\text{)}$	$\log \xi$	$r \text{ (cm)}$	$\Delta r \text{ (cm)}$	$v \text{ (km s}^{-1}\text{)}$
Blobs	Compton-thick core	$\sim 2 \times 10^{12}$	0.1	$\sim 10^{15}$	$\sim 1 \times 10^{12}$	-650
	Ionized layer (WA1)	$\sim 7 \times 10^{10}$	1.5		$\sim 1 \times 10^{11}$	
Line-driven disc winds	WA2	$\sim 10^{10}$	2.5	$\sim 4 \times 10^{14}$	$\sim 9 \times 10^{11}$	-4100
	WA3	$\gtrsim 2 \times 10^9$	3.4	$\gtrsim 3 \times 10^{14}$	$\gtrsim 3 \times 10^{14}$	-6100


Figure 14. Fitting of the F_{var} spectra with the simulated ones when the ionization degree of WA1 varies.

show little variability. The double-layer absorbers are composed of the Compton-thick core and the ionized outer layer, located at $\sim 10^3 R_s$, and partially cover the central X-ray source. The partial covering fraction varies significantly, which is the prime origin of the observed X-ray spectral/flux variation.

5 CONCLUSION

We have analysed the *XMM-Newton* archival data of NLS1 NGC 4051. X-ray energy spectra have at least three distinct warm absorber outflows; WA1 ($\log \xi = 1.5, v = -650 \text{ km s}^{-1}$), WA2 ($\log \xi = 2.5, v = -4100 \text{ km s}^{-1}$) and WA3 ($\log \xi = 3.4, v = -6100 \text{ km s}^{-1}$). The long enough exposure time has enabled us to calculate the rms spectra with the RGS energy resolution for the first time. Consequently, we have found that the rms spectra have a sharp peak and dips, which can be explained by variable absorption features and non-variable emission lines. The Fe-L UTA created by WA1 shows large variability at a time-scale of $\sim 10^4 \text{ s}$, which suggests that WA1 locates at $\sim 10^3 R_s$. The depth of Fe-L UTA and the soft X-ray flux often show anticorrelation, which can be explained by variable partial covering fraction of the double-layer blobs that have the Compton-thick core responsible for the soft X-ray flux variation and the ionized layer (=WA1) responsible for the Fe-L UTA, whereas the intrinsic luminosity is hardly variable. On the other hand, WA2 and WA3 show little variability; they presumably extend uniformly in the line of sight, and locate at several hundred R_s . Physical parameters of WA2 and WA3 are reproduced by numerical simulation of the line-driven disc winds. In summary, we propose that NGC 4051 has two types of the warm absorber outflows: the static, high-ionized

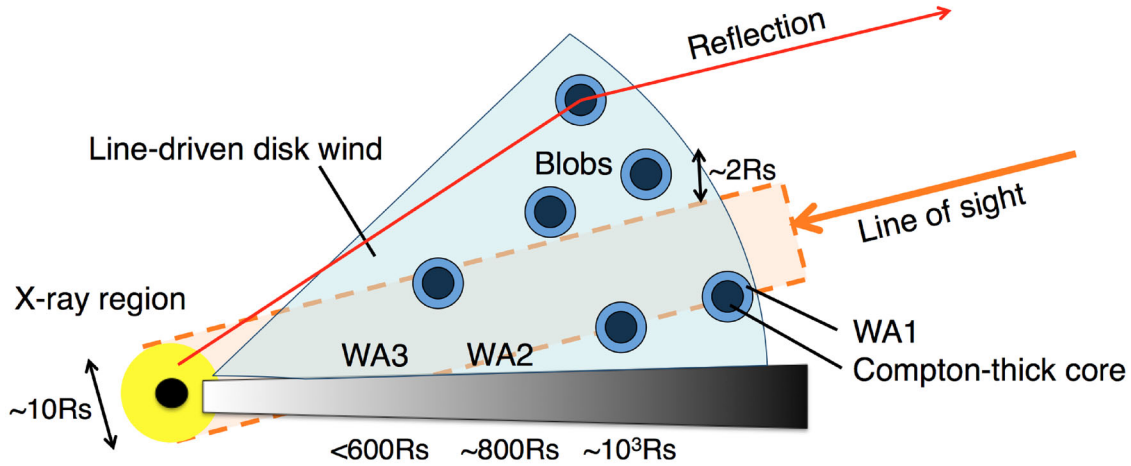


Figure 15. Schematic picture of geometry of warm absorber outflows in NGC 4051

and extended line-driven disc winds and the variable, low-ionized and clumpy double-layer blobs.

ACKNOWLEDGEMENTS

This work is based on observations obtained with *XMM-Newton*, an ESA science mission with instruments and contributions directly funded by ESA Member States and NASA. We used public data obtained through the High Energy Astrophysics Science Archive Research Center (HEASARC) at NASA/GSFC, and software provided by HEASARC at NASA/GSFC for data reduction. MM and KE are financially supported by the JSPS KAKENHI Grant Number JP15J07567 and JP16K05309, respectively.

REFERENCES

- Arnaud K. A., 1996, in Jacoby G. H., Barnes J., eds, ASP Conf. Ser. Vol. 101, *Astronomical Data Analysis Software and Systems V*. Astron. Soc. Pac., San Francisco, p. 17
- Balucinska-Church M., McCammon D., 1992, *ApJ*, 400, 699
- Behar E., Sako M., Kahn S. M., 2001, *ApJ*, 563, 497
- Collinge M. J. et al., 2001, *ApJ*, 557, 2
- Czerny B., Nikolaćuk M., Piasecki M., Kuraszkiewicz J., 2001, *MNRAS*, 325, 865
- Den Herder J. et al., 2001, *A&A*, 365, L7
- Denney K. D. et al., 2009, *ApJ*, 702, 1353
- Dere K. P., Landi E., Young P. R., Del Zanna G., 2001, *ApJS*, 134, 331
- Edelson R., Turner T. J., Pounds K., Vaughan S., Markowitz A., Marshall H., Dobbie P., Warwick R., 2002, *ApJ*, 568, 610
- Elvis M., Wilkes B. J., Lockman F. J., 1989, *AJ*, 97, 777
- Haba Y., Liebmann A. C., Fukumura K., Kunieda H., Tsuruta S., 2008, *PASJ*, 60, 1257
- Iso N., Ebisawa K., Sameshima H., Mizumoto M., Miyakawa T., Yamasaki H., Inoue H., 2016, *PASJ*, 68, S27
- Jansen F. et al., 2001, *A&A*, 365, L1
- Kaastra J. S. et al., 2014, *Science*, 345, 64
- Kallman T. R., Palmeri P., Bautista M. A., Mendoza C., Krolik J. H., 2004, *ApJS*, 155, 675
- King A. L., Miller J. M., Raymond J., 2012, *ApJ*, 746, 2
- Krongold Y., Nicastro F., Elvis M., Brickhouse N., Binette L., Mathur S., Jiménez-Bailón E., 2007, *ApJ*, 659, 1022
- Kunieda H., Hayakawa S., Tawara Y., Koyama K., Tsuruta S., Leighly K., 1992, *ApJ*, 384, 482
- Lobban A. P., Reeves J. N., Miller L., Turner T. J., Braitto V., Kraemer S. B., Crenshaw D. M., 2011, *MNRAS*, 414, 1965
- Magdziarz P., Zdziarski A. A., 1995, *MNRAS*, 273, 837
- Maiolino R. et al., 2010, *A&A*, 517, A47
- Miller L., Turner T. J., Reeves J. N., 2009, *MNRAS*, 399, L69
- Miller L., Turner T. J., Reeves J. N., Lobban A., Kraemer S. B., Crenshaw D. M., 2010, *MNRAS*, 403, 196
- Mitsuda K. et al., 1984, *PASJ*, 36, 741
- Miyakawa T., Ebisawa K., Inoue H., 2012, *PASJ*, 64, 140
- Mizumoto M., Ebisawa K., Sameshima H., 2014, *PASJ*, 66, 122
- Nandra K., O'Neill P. M., George I. M., Reeves J. N., 2007, *MNRAS*, 382, 194
- Nicastro F., Fiore F., Perola G. C., Elvis M., 1999, *ApJ*, 512, 184
- Nomura M., Ohsuga K., Takahashi H. R., Wada K., Yoshida T., 2016, *PASJ*, 68, 16
- Nucita A. A., Guainazzi M., Longinotti A. L., Santos-Lleo M., Maruccia Y., Bianchi S., 2010, *A&A*, 515, A47
- Ponti G., Miniutti G., Cappi M., Maraschi L., Fabian A. C., Iwasawa K., 2006, *MNRAS*, 368, 903
- Pounds K. A., Vaughan S., 2011a, *MNRAS*, 413, 1251
- Pounds K. A., Vaughan S., 2011b, *MNRAS*, 415, 2379
- Pounds K. A., Reeves J. N., King A. R., Page K. L., 2004, *MNRAS*, 350, 10
- Proga D., Stone J. M., Kallman T. R., 2000, *ApJ*, 543, 686
- Silva C., Uttley P., Costantini E., 2016, *A&A*, 596, A79
- Steenbrugge K. C., Fenovčík M., Kaastra J. S., Costantini E., Verbunt F., 2009, *A&A*, 496, 107
- Strüder L. et al., 2001, *A&A*, 365, L18
- Terashima Y. et al., 2009, *PASJ*, 61, S299
- Wilms J., Allen A., McCray R., 2000, *ApJ*, 542, 914
- Yamasaki H., Mizumoto M., Ebisawa K., Sameshima H., 2016, *PASJ*, 68, 80
- Yan M., Sadeghpour H. R., Dalgarno A., 1998, *ApJ*, 496, 1044

APPENDIX A: rms CALCULATION

Consider a light curve divided into N time bins. The fractional variability amplitude F_{var} is calculated to be

$$F_{\text{var}} = \frac{\sqrt{\frac{1}{N} \sum_{i=1}^N (F_i - \langle F \rangle)^2}}{\langle F \rangle}, \quad (\text{A1})$$

where F_i is the observed X-ray flux in the i th bin, and $\langle F \rangle$ is the mean value of F_i .

A1 Effect of N_{H} variation

Passing through an X-ray absorber, F_i is expressed as

$$F_i = e^{-\sigma N_{\text{H},i}} F_{\text{int}}, \quad (\text{A2})$$

where σ is a cross-section, $N_{\text{H},i}$ is column density in the i th bin and F_{int} is the intrinsic X-ray flux.

When $\tau_i = \sigma N_{\text{H},i} \ll 1$ and the warm absorber is optically thin,

$$F_i \simeq (1 - \sigma N_{\text{H},i}) F_{\text{int}}. \quad (\text{A3})$$

Thus, equation (A1) is calculated to be

$$\begin{aligned} F_{\text{var}} &\simeq \frac{\sqrt{\frac{1}{N} \sum_{i=1}^N ((1 - \sigma N_{\text{H},i}) - (1 - \sigma N_{\text{H}}))^2}}{(1 - \sigma N_{\text{H}})} \\ &= \frac{\sqrt{\frac{1}{N} \sum_{i=1}^N (\sigma N_{\text{H},i} - \langle \sigma N_{\text{H}} \rangle)^2}}{(1 - \sigma N_{\text{H}})} \\ &= \frac{\sqrt{\frac{1}{N} \sum_{i=1}^N (\sigma N_{\text{H},i} - \langle \sigma N_{\text{H}} \rangle)^2}}{\langle \sigma N_{\text{H}} \rangle} \cdot \frac{\langle \sigma N_{\text{H}} \rangle}{(1 - \sigma N_{\text{H}})} \\ &= (\sigma N_{\text{H}})_{\text{var}} \cdot \frac{\sigma \langle N_{\text{H}} \rangle}{1 - \sigma \langle N_{\text{H}} \rangle} \\ &= (N_{\text{H}})_{\text{var}} \cdot \frac{\sigma \langle N_{\text{H}} \rangle}{1 - \sigma \langle N_{\text{H}} \rangle} \\ &= (N_{\text{H}})_{\text{var}} \cdot \frac{\langle \tau \rangle}{1 - \langle \tau \rangle}. \quad (\text{A4}) \end{aligned}$$

Equation (A4) monotonically increases on σ when $\langle \tau \rangle < 1$. $(N_{\text{H}})_{\text{var}}$ is proportional to the variable range of $N_{\text{H},i}$ ($=\Delta N_{\text{H}}$). When $N_{\text{H},i}$ monotonically varies within $[\langle N_{\text{H}} \rangle - \Delta N_{\text{H}} : \langle N_{\text{H}} \rangle + \Delta N_{\text{H}}]$, $(N_{\text{H}})_{\text{var}} = \frac{1}{\sqrt{3}} (\Delta N_{\text{H}} / \langle N_{\text{H}} \rangle)$.

A2 Effect of partial-covering-fraction variation

When a warm absorber is optically thin, the change of N_{H} is equivalent to the change of partial covering fraction (see equation 6). Thus, F_i is expressed as

$$\begin{aligned} F_i &= (1 - \alpha_i + \alpha_i \exp[-\sigma N_{\text{H}}^{\text{fixed}}]) F_{\text{int}} \\ &\equiv (1 - \alpha_i + \alpha_i W_f) F_{\text{int}}. \quad (\text{A5}) \end{aligned}$$

Thus, equation (A1) is calculated as

$$\begin{aligned} F_{\text{var}} &= \frac{\sqrt{\frac{1}{N} \sum_{i=1}^N \{(1 - \alpha_i + \alpha_i W_f) - (1 - \alpha + \alpha W_f)\}^2}}{(1 - \alpha + \alpha W_f)} \\ &= \frac{\sqrt{\frac{1}{N} \sum_{i=1}^N (-1 + W_f)^2 (\alpha_i - \langle \alpha \rangle)^2}}{1 - \langle \alpha \rangle + \langle \alpha \rangle W_f} \\ &= \frac{\sqrt{\frac{1}{N} \sum_{i=1}^N (\alpha_i - \langle \alpha \rangle)^2}}{\langle \alpha \rangle} \cdot \frac{(1 - W_f) \langle \alpha \rangle}{1 - (1 - W_f) \langle \alpha \rangle} \\ &= (\alpha)_{\text{var}} \cdot \frac{(1 - \exp[-\sigma N_{\text{H}}^{\text{fixed}}]) \langle \alpha \rangle}{1 - (1 - \exp[-\sigma N_{\text{H}}^{\text{fixed}}]) \langle \alpha \rangle}. \quad (\text{A6}) \end{aligned}$$

A3 Effect of an emission line

When a non-variable component (such as an emission line) exists, rms at the energy band decreases. Assuming that the X-ray flux consists of a variable component A and an invariant component B , F_i is expressed as

$$F_i = A_i + B. \quad (\text{A7})$$

Here,

$$\begin{aligned} F_{\text{var}} &= \frac{\sqrt{\frac{1}{N} \sum_{i=1}^N (A_i + B - \langle A + B \rangle)^2}}{\langle A + B \rangle} \\ &= \frac{\sqrt{\frac{1}{N} \sum_{i=1}^N (A_i - \langle A \rangle)^2}}{\langle A \rangle + B} \\ &= A_{\text{var}} \cdot \frac{\langle A \rangle}{\langle A \rangle + B} \\ &= A_{\text{var}} \cdot \frac{1}{1 + x}, \quad (\text{A8}) \end{aligned}$$

where x is the intensity ratio of the invariant component to the variable component ($=B/\langle A \rangle$).

This paper has been typeset from a $\text{\TeX}/\text{\LaTeX}$ file prepared by the author.